International Journal of
Molecular Sciences

MDPI

Article

Product Distributions of Cytochrome P450 $OleT_{JE}$ with Phenyl-Substituted Fatty Acids: A Computational Study

Yen-Ting Lin [1,2] and Sam P. de Visser [1,2,*]

[1] Manchester Institute of Biotechnology, The University of Manchester, Manchester M1 7DN, UK; yen-ting.lin@manchester.ac.uk
[2] Department of Chemical Engineering and Analytical Science, The University of Manchester, Manchester M13 9PL, UK
* Correspondence: sam.devisser@manchester.ac.uk

Abstract: There are two types of cytochrome P450 enzymes in nature, namely, the monooxygenases and the peroxygenases. Both enzyme classes participate in substrate biodegradation or biosynthesis reactions in nature, but the P450 monooxygenases use dioxygen, while the peroxygenases take H_2O_2 in their catalytic cycle instead. By contrast to the P450 monooxygenases, the P450 peroxygenases do not require an external redox partner to deliver electrons during the catalytic cycle, and also no external proton source is needed. Therefore, they are fully self-sufficient, which affords them opportunities in biotechnological applications. One specific P450 peroxygenase, namely, P450 $OleT_{JE}$, reacts with long-chain linear fatty acids through oxidative decarboxylation to form hydrocarbons and, as such, has been implicated as a suitable source for the biosynthesis of biofuels. Unfortunately, the reactions were shown to produce a considerable amount of side products originating from C^{α} and C^{β} hydroxylation and desaturation. These product distributions were found to be strongly dependent on whether the substrate had substituents on the C^{α} and/or C^{β} atoms. To understand the bifurcation pathways of substrate activation by P450 $OleT_{JE}$ leading to decarboxylation, C^{α} hydroxylation, C^{β} hydroxylation and C^{α}–C^{β} desaturation, we performed a computational study using 3-phenylpropionate and 2-phenylbutyrate as substrates. We set up large cluster models containing the heme, the substrate and the key features of the substrate binding pocket and calculated (using density functional theory) the pathways leading to the four possible products. This work predicts that the two substrates will react with different reaction rates due to accessibility differences of the substrates to the active oxidant, and, as a consequence, these two substrates will also generate different products. This work explains how the substrate binding pocket of P450 $OleT_{JE}$ guides a reaction to a chemoselectivity.

Keywords: biocatalysis; enzyme mechanism; cytochrome P450; hydroxylation; desaturation; biofuel

Citation: Lin, Y.-T.; de Visser, S.P. Product Distributions of Cytochrome P450 $OleT_{JE}$ with Phenyl-Substituted Fatty Acids: A Computational Study. *Int. J. Mol. Sci.* **2021**, *22*, 7172. https://doi.org/10.3390/ijms22137172

Academic Editor: Antonio Trincone

Received: 14 June 2021
Accepted: 29 June 2021
Published: 2 July 2021

1. Introduction

With the advent of knowledge on biochemical reaction processes and mechanisms, the use of biosystems in engineering processes has increased rapidly. In particular, enzymes are now commonly applied in industrial processes related to food production as well as the synthesis of fine-chemicals. One area of great potential for enzymes is the field of biofuels, where they can be utilized for the synthesis of hydrocarbons. Interestingly, in nature, there are several enzymes involved in the conversion of alcohols or fatty acids into hydrocarbons [1–6], and, as such, there is potential to use these for biotechnical applications. Most of these enzymes are metalloenzymes, where a reaction on either an iron or copper center takes place. Metalloenzymes are highly versatile in nature and catalyze substrate oxidation and reduction reactions efficiently [7–9]. In particular, the oxygen-activating mononuclear iron-containing enzymes are useful in this respect. They have been assigned to two different categories, namely, the heme monooxygenases [10–18] and the nonheme

iron dioxygenases [19–26], where the former group includes the cytochromes P450 involved in biosynthesis and biodegradation processes.

The cytochromes P450 are heme enzymes that either take O_2 and react as monooxygenases or use H_2O_2 and operate as peroxygenases. P450 monooxygenases react dioxygen on an iron (III)-heme center to form an iron (IV)-oxo heme cation radical species called Compound I (CpdI) with the help of two external electrons (from redox partners) and two protons from the solvent according to the mechanism shown in Scheme 1. CpdI is a versatile catalyst that reacts with aliphatic chains through substrate hydroxylation or desaturation, or with olefins and arenes to form epoxides and phenols. In addition to the P450 monooxygenases, there are several P450s that use H_2O_2 instead of dioxygen and therefore act as peroxygenases. These also form CpdI in their catalytic cycle but do not need external electrons and protons as they are provided by H_2O_2 (bottom reaction in Scheme 1). As such, these P450 peroxygenases are self-sufficient and more suitable for biotechnological applications than the P450 monooxygenases. The P450 peroxygenases were reported to take long-chain fatty acids as substrates and react them through an oxidative decarboxylation to form terminal olefins [27–37].

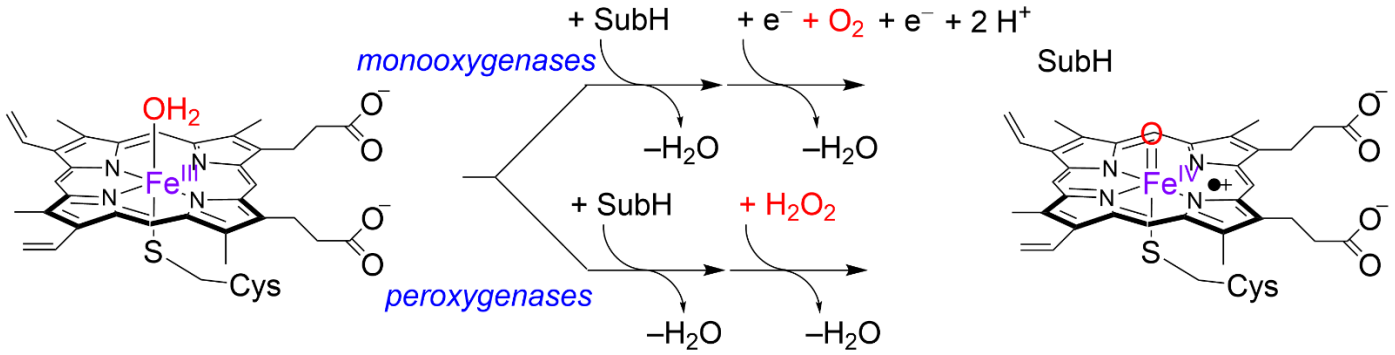

Scheme 1. Reaction mechanism for the formation of the active species in cytochrome P450 enzymes (Compound I) in monooxygenases using dioxygen (top reaction) or in peroxygenases using H_2O_2 (lower reaction); SubH is the substrate.

P450 peroxygenases were also shown to react with a variety of small carboxylic acids; however, the product distributions were markedly different between the various substrates [36]. Thus, Pickl et al. [36] showed that P450 $OleT_{JE}$ reacts with linear fatty acids, and, e.g., a substrate with the chain length of 13 carbon atoms produced dominant decarboxylation products to form the C_{12} olefin with a minor amount of C^{β} hydroxylation. By contrast, using *R*- or *S*-2-methylbutyrate instead, P450 $OleT_{JE}$ converted the substrate to the C^{α}-hydroxylated product or caused desaturation of the C^{α}–C^{β} bond. Computational modeling on the mechanism of the latter reaction showed that the substrate was able to bind in various conformations that led to different reaction channels and products that are close in energy [36,38]. Yet, when P450 $OleT_{JE}$ was fed with 2-methyl-3-phenylpropionate, the reaction products corresponded to decarboxylation and C^{α} hydroxylation instead [36], as shown in Scheme 2. By contrast, the reaction of P450 $OleT_{JE}$ with 2-phenylbutyrate gave a major reaction channel for C^{α} hydroxylation and a minor amount of C^{α}–C^{β} desaturation. Clearly, the reaction products of substrate activation by P450 $OleT_{JE}$ are highly dependent on the size and shape of the substrate, and the origins of these product distributions remain unclear. Therefore, we decided to conduct another computational study into substrate activation by P450 $OleT_{JE}$, investigate substrates with phenyl substituents and find out how P450 $OleT_{JE}$ would activate these. In particular, no computational studies have been reported on fatty acids with phenyl side chains that create bulkier substrates than linear long-chain fatty acids and hence may not fit the substrate binding pocket well.

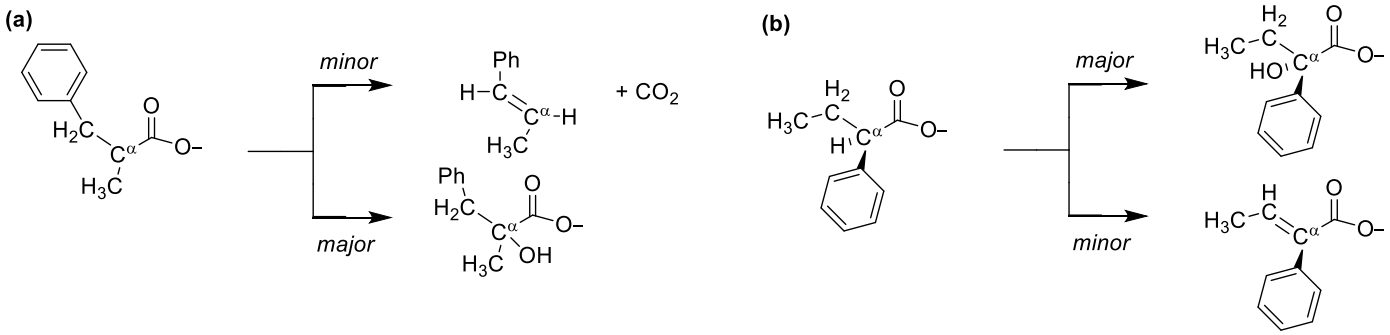

Scheme 2. Substrate activation of phenyl-substituted fatty acids by P450 OleTJE: (**a**) Activation of 2-methyl-3-phenylpropionate. (**b**) Activation of 2-phenylbutyrate.

2. Results

To understand the mechanism of substrate activation by P450 $OleT_{JE}$ enzymes and, in particular, how the enzymes react with fatty acid substrates with phenyl substituents, we decided to create a series of cluster models and study the possible reaction pathways for fatty acid activation by CpdI models. Several previous studies covered the H_2O_2 activation on a heme center to form CpdI [39–42], which is the active oxidant that performs the catalysis. Hence, we will focus on the mechanism starting from CpdI and a substrate only. Previous studies of ours showed that large QM cluster models of well over 150 atoms represent the oxidant and substrate binding pockets of enzymes highly accurately and give results at par with QM/MM methods [43–46]. Therefore, a large QM cluster model of the substrate-bound P450 OleT models was set up. The substrate-bound structure of P450 $OleT_{JE}$ was characterized crystallographically by Belcher et al. [47], and an extract of the 4L40 protein databank file [48] (pdb) is shown in Figure 1. As it can be seen, the heme is linked to the protein through a thiolate linkage of Cys_{365}. The substrate binding pocket is mostly lined with aromatic and aliphatic amino acids including the side chains of Leu_{78}, Phe_{79}, Ile_{170}, Pro_{246} and Phe_{291}. In the substrate binding pocket, the carboxylate of the icosanoic acid substrate forms a salt bridge with the side chain of Arg_{245}.

To understand the substrate activation mechanism, we set up cluster models using previously reported methods that take key hydrogen bonding and polar residues into consideration [49,50]. In order to do so, we removed the icosanoic acid from the pdb and docked an alternative substrate manually into the pocket. These substrates lack the long aliphatic tail of icosanoic acid, and hence the models we created only included protein residues within the vicinity of the new substrates. In particular, we created two reactant models, namely, $\mathbf{Re}_{S1}$ and $\mathbf{Re}_{S2}$, which have the same protein structure but contain a different substrate, i.e., either **S1** or **S2**, Figure 1b. Thus, substrate **S1** is 3-phenylpropionate and substrate **S2** is 2-phenylbutyrate. Model $\mathbf{Re}_{S1}$ has 162 atoms in total, whereas model $\mathbf{Re}_{S2}$ contains 165 atoms. Both systems have a neutral charge and were calculated in the lowest energy doublet and quartet spin states, as identified with the superscript of 2 or 4 next to the labels. Following previous experience with substrate binding into the active site of P450 $OleT_{JE}$ [36], we made sure the substrate forms a double hydrogen bonding interaction and salt bridge of its carboxylate group with the methylguanidinium group of Arg_{245}. In addition, the model contains the heme with all ring substituents truncated to hydrogen atoms and the axial Cys_{365} residue as thiolate. The substrate binding pocket contains the peptide dimers Leu_{78}-Phe_{79} and Arg_{245}-Pro_{246} as well as the side chains of residues Ile_{170} and Phe_{291}. A previous study used the same peptide and active site model but with hexanoate as substrate [38], whereby the model was validated against high-level quantum mechanics/molecular mechanics (QM/MM) calculations [51,52] and large cluster models [53]. These studies found very good agreement of the calculations of energy landscapes for a reaction mechanism, as obtained with either cluster models or QM/MM. In addition, a range of computational methods were tested, namely, several density functional theory methods and basis sets, and all approaches came to the same conclusions and

predicted similar rate constants. As such, we will use large cluster models here with the B3LYP method in combination with a double-ζ quality basis set on all atoms, i.e., LACVP basis set with core potential on iron and 6-31G on the rest of the atoms, while a solvent model with a dielectric constant of ε = 5.7 was included in the geometry optimizations, as well, as that enables a comparison with previous work in the field.

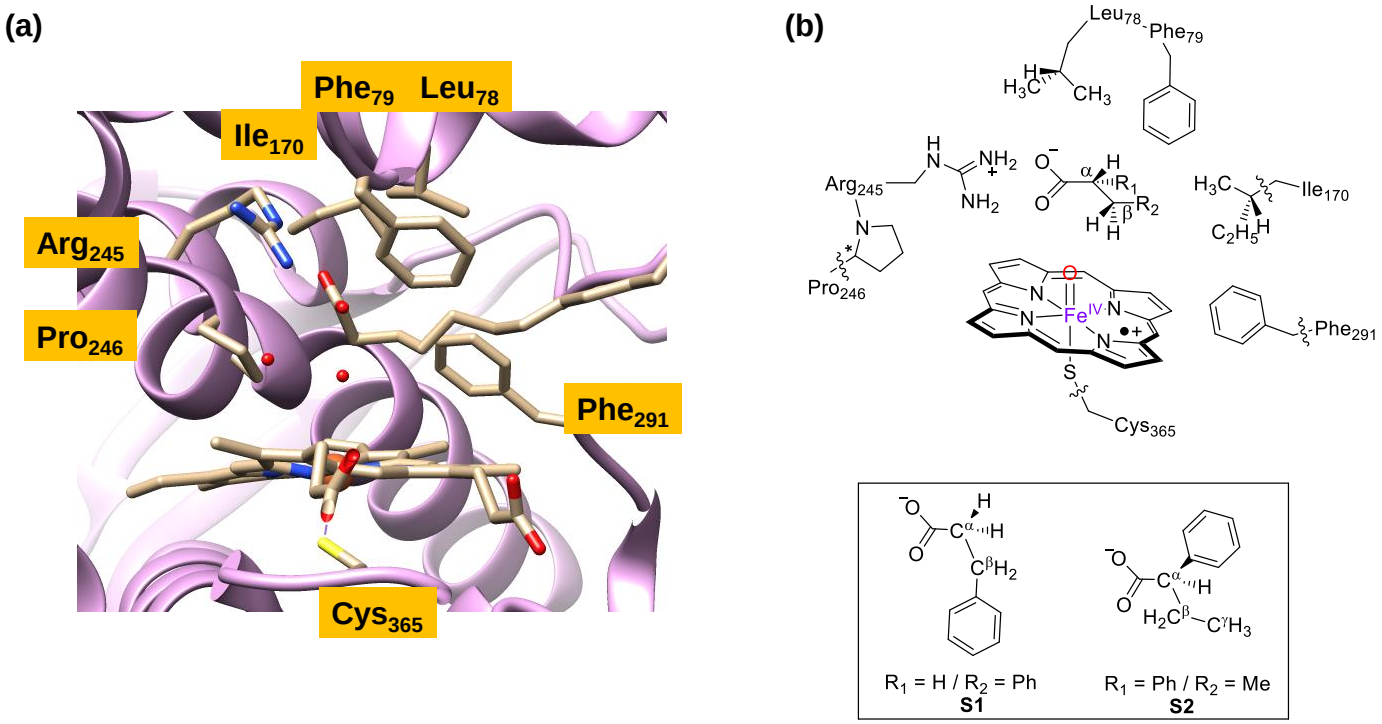

Figure 1. (**a**) Active site of the crystal structure coordinates of the substrate-bound form of P450 $OleT_{JE}$ from the 4L40 protein databank file with key residues highlighted; (**b**) cluster models of the active site of P450 $OleT_{JE}$ as investigated in this work with the substrates S1 and S2 shown in the inset.

The optimized geometry of our CpdI model with substrate **S1** bound (**Re**$_{S1}$) is shown in Figure 2a for the doublet and quartet spin states. Geometrically, the doublet and quartet spin state structures are very similar with almost equal Fe–O distances of 1.665 and 1.654 Å and Fe–S interactions of 2.553 and 2.571 Å, respectively. This is not surprising as the two spin states are known to be close in energy [54–60] in CpdI and have the same orbital occupation with three unpaired electrons in orbitals labeled a_{2u}, π^*_{xz} and π^*_{yz} (Figure 2b). The a_{2u} orbital is a heme-based orbital that in D_{4h} symmetry has contributions on the pyrrole nitrogen atoms and the *meso*-carbon atoms. In addition, it mixes strongly with a lone pair orbital on the sulfur atom of the axial ligand, which gives it its oxidative power. The π^*_{xz} and π^*_{yz} orbitals are the antibonding orbitals along the Fe–O bond. Similar structures and orbital occupations were obtained for the reactant complexes with substrate **S2** bound (**Re**$_{S2}$). Overall, the reactant structure and electronic configuration match previous computational studies on P450 CpdI excellently and predict similar bond lengths to those seen previously for analogous systems [36,38,51–78].

Next, we explored the substrate activation channels of **S1** and **S2** by CpdI, and the details of the explored reaction mechanisms are shown in Scheme 3 with the designated labeling of the individual structures. Thus, structures related to substrate **S1** have S1 in subscript after the label, while those associated with substrate **S2** have S2 in subscript after the label. In particular, we tested the activation of the C^{α}–H and C^{β}–H bonds of both substrates, while for **S2**, we also investigated the products originating from C^{γ}–H activation. These reaction pathways start with an initial hydrogen atom abstraction from either the C^{α}–H, C^{β}–H or C^{γ}–H (if applicable) positions via transition states **TS1**$_{HA,\alpha}$, **TS1**$_{HA,\beta}$ and **TS1**$_{HA,\gamma}$ to form the radical intermediates designated **IM1**$_{\alpha}$, **IM1**$_{\beta}$ and **IM1**$_{\gamma}$.

As it is usually seen in substrate hydroxylation pathways [55,79,80], an OH rebound barrier via $\mathbf{TS2}_{reb,\alpha}$, $\mathbf{TS2}_{reb,\beta}$ or $\mathbf{TS2}_{reb,\gamma}$ then gives C^{α} hydroxylation, C^{β} hydroxylation and C^{γ} hydroxylation products ($\mathbf{Pr}_{OH,\alpha}$, $\mathbf{Pr}_{OH,\beta}$ and $\mathbf{Pr}_{OH,\gamma}$), respectively. In addition, from either $\mathbf{IM1}_{\alpha}$ or $\mathbf{IM1}_{\beta}$ a second hydrogen atom abstraction can take place via transition states $\mathbf{TS2}_{DS,\alpha}$ and $\mathbf{TS2}_{DS,\beta}$ to form a double bond along the C^{α}–C^{β} bond and give a desaturated product ($\mathbf{Pr}_{DS}$). A final mechanism through substrate decarboxylation is only possible from $\mathbf{IM1}_{\beta}$ via transition state $\mathbf{TS2}_{DC}$ to form CO_2, olefin and an iron(III)–hydroxo(heme) complex, $\mathbf{Pr}_{DC}$. We investigated all these individual reaction pathways for the cluster model **Re** with substrates **S1** and **S2** bound in the quartet spin state as previous work showed the quartet spin state to be the most sensitive to bifurcation pathways [52,81].

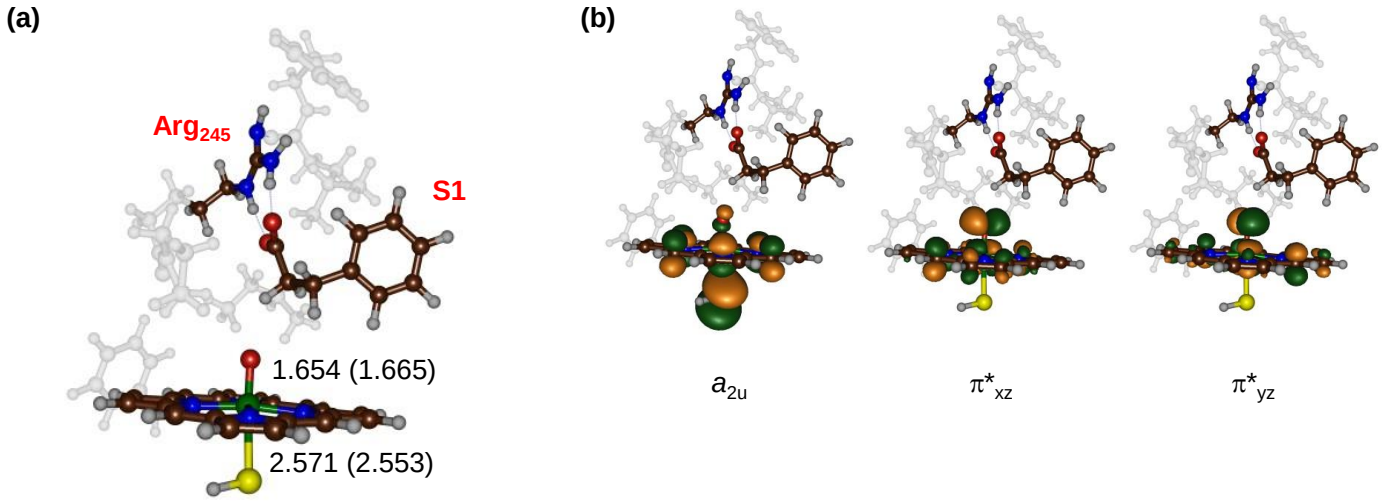

Figure 2. (**a**) Optimized geometries of the **S1**-bound reactant complexes $^{4}\mathbf{Re}_{S1}$ ($^{2}\mathbf{Re}_{S1}$) with bond lengths in angstroms; (**b**) singly occupied molecular orbitals of $^{4,2}\mathbf{Re}_{S1}$.

2.1. 3-Phenylpropionate Activation by CpdI of P450 OleT$_{JE}$

Next, a mechanistic study into 3-phenylpropionate (**S1**) activation by the CpdI model of P450 $OleT_{JE}$ was performed using model $\mathbf{Re}_{S1}$ leading to decarboxylation, desaturation, α-hydroxylation and β-hydroxylation products, as described above in Scheme 3. These four reaction products all originate from either C^{α}–H or C^{β}–H hydrogen atom abstraction; hence, we will start with the hydrogen atom abstraction steps first. Figure 3 shows the hydrogen atom abstraction transition state structures $\mathbf{TS1}_{HA,\alpha,S1}$ and $\mathbf{TS1}_{HA,\beta,S1}$ as geometries optimized with density functional theory methods. In addition, the middle panel of Figure 3 shows the energy profile for relative enthalpies (ΔE+ZPE; ZPE = zero-point energy). The C^{β}–H hydrogen atom abstraction barrier is considerably lower in energy than the C^{α}–H hydrogen atom abstraction barrier: ΔE+ZPE = 14.6 kcal mol^{-1} for $\mathbf{TS1}_{HA,\beta,S1}$ and ΔE+ZPE = 20.9 kcal mol^{-1} for $\mathbf{TS1}_{HA,\alpha,S1}$. Therefore, **S1** activation by CpdI of P450 $OleT_{JE}$ will give dominant products from C^{β}–H activation. The barrier for $\mathbf{TS1}_{HA,\beta,S1}$ is close in energy to the one calculated by a minimal cluster model without protein residues for C^{β}–H activation of propane or the activation of the methyl C–H bond of *trans*-methyl-phenylcyclopropane [82–84]. The fact that the barrier $\mathbf{TS1}_{HA,\alpha,S1}$ is much higher in energy than those barriers obtained with the minimal model and *trans*-methyl-phenylcyclopropane means that the second coordination sphere of the enzyme, i.e., the substrate binding pocket, restricts the substrate positioning and hampers C^{α}–H hydrogen atom abstraction dramatically, raising it in energy.

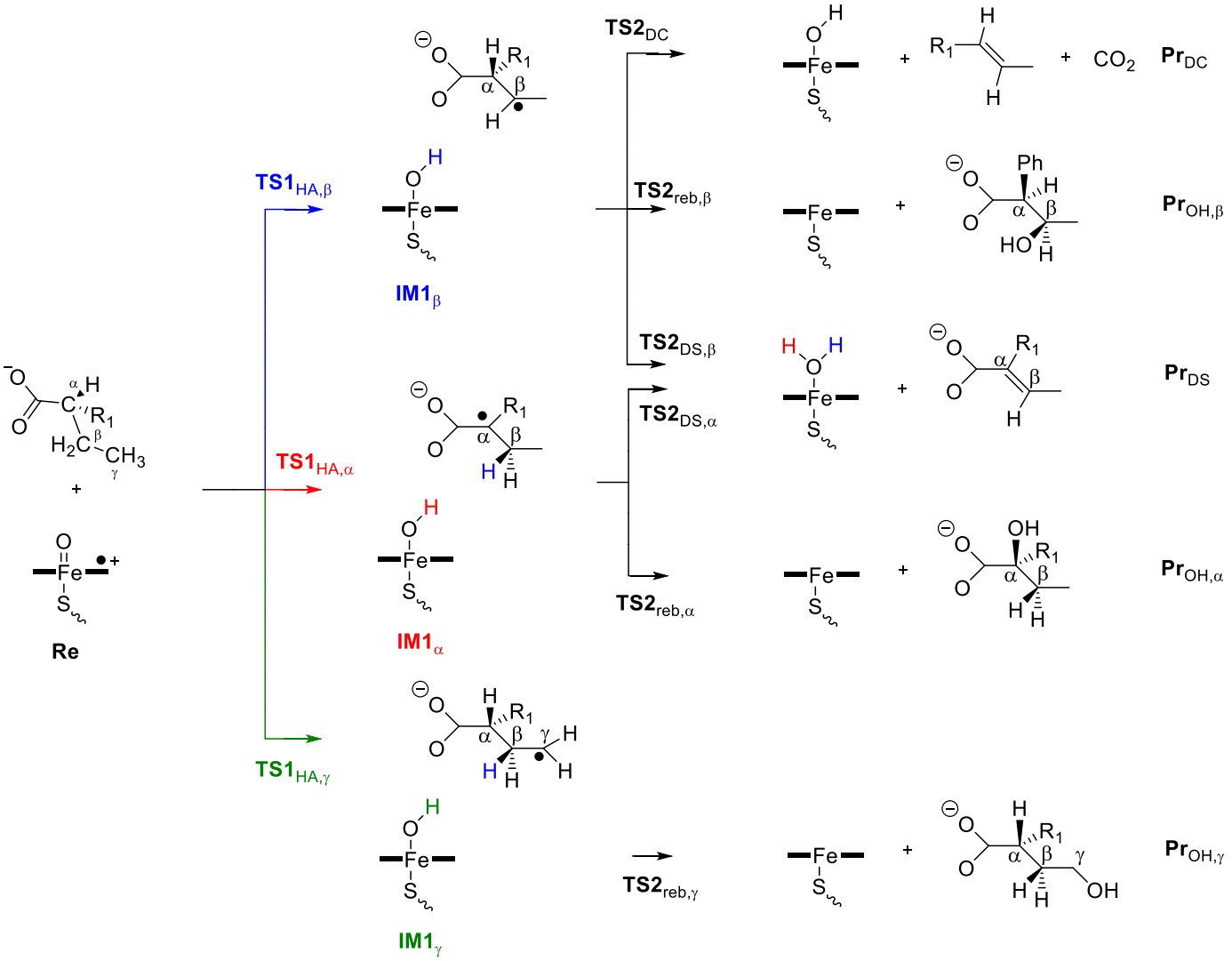

Scheme 3. Reaction mechanisms explored for substrate activation by P450 $OleT_{JE}$ with definition of the labels for the intermediates, products and transition states.

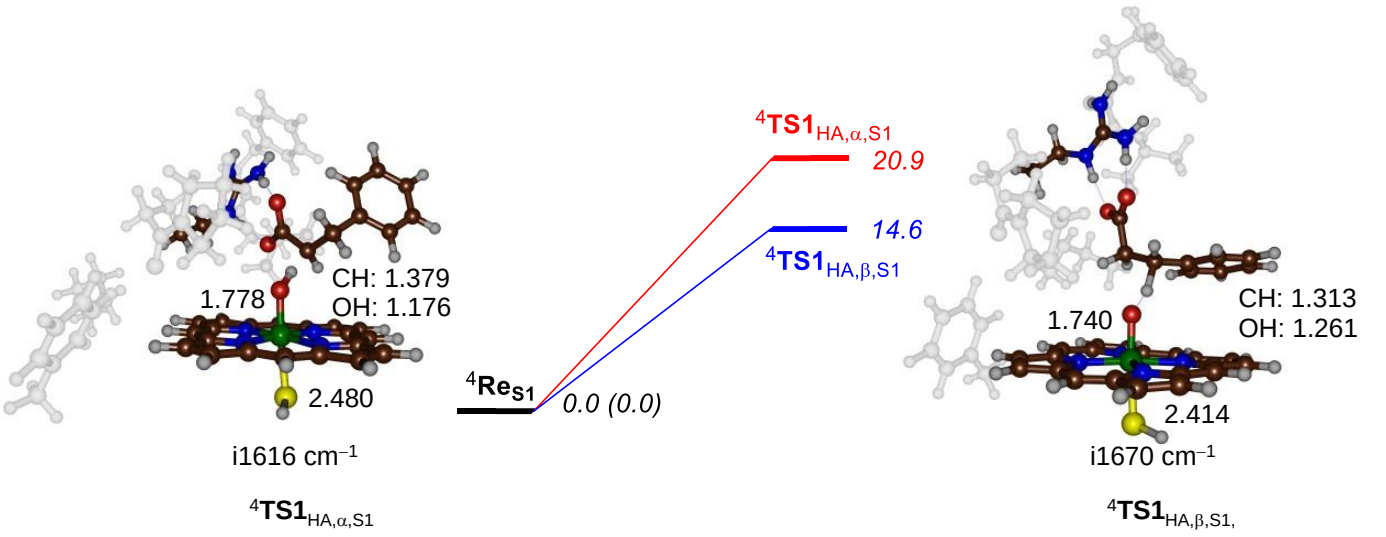

Figure 3. Hydrogen atom abstraction steps from substrate **S1** by CpdI of P450 $OleT_{JE}$. The middle panel shows relative energies in kcal mol^{-1} as obtained at the ΔE_{BS2}+ZPE_{BS1} level of theory. Hydrogen atom abstraction transition state structures are shown on the side with bond lengths in angstroms and the imaginary frequency in the transition state in cm^{-1}.

In general, both transition state structures are late, with long C–H bonds of 1.379 Å (**TS1**$_{HA,\alpha,S1}$) and 1.313 Å (**TS1**$_{HA,\beta,S1}$), whereas the accepting O–H bond is much shorter: 1.176 Å for **TS1**$_{HA,\alpha,S1}$ and 1.261 Å for **TS1**$_{HA,\beta,S1}$. In both transition states, the Fe–O distance has elongated from 1.654 in the reactant complex to 1.778 Å in **TS1**$_{HA,\alpha,S1}$ and 1.740 Å in **TS1**$_{HA,\beta,S1}$. This is due to the formation of the O–H bond which polarizes the π^*_{yz} orbital more to the iron and hence makes the Fe–O bond weaker. Both transition states are characterized by a large imaginary frequency for the O–H–C stretch vibration, with a magnitude of i1616 cm^{-1} (**TS1**$_{HA,\alpha,S1}$) and i1670 cm^{-1} (**TS1**$_{HA,\beta,S1}$). These large imaginary frequencies implicate that the potential energy surface is steep and gives a narrow-width peak that could result in a large kinetic isotope effect due to quantum mechanical tunneling and that will be sensitive to the substitution of hydrogen by deuterium atoms.

The transition states relax to radical intermediates **IM1**$_{\alpha,S1}$ and **IM1**$_{\beta,S1}$ that react further past the various bifurcation channels. Let us start with the pathways from **IM1**$_{\alpha,S1}$ that can lead to desaturation of the C$^{\alpha}$–C$^{\beta}$ bond via a second hydrogen atom abstraction or OH rebound to give the alcohol product complex; the optimized geometries and the energy landscape are shown in Figure 4. The **IM1**$_{\alpha,S1}$ intermediate is only 1 kcal mol^{-1} higher in energy than the reactant complex **Re**$_{S1}$ and has the transition states leading to the two reaction pathways to products within 2 kcal mol^{-1}. In particular, the lowest barrier leads to desaturation through a second hydrogen atom abstraction from C$^{\beta}$–H via a transition state of ΔE+ZPE = 15.7 kcal mol^{-1}. By contrast, the OH rebound barrier is ΔE+ZPE = 17.3 kcal mol^{-1}. These close barriers implicate that a mixture of products may be expected for **S1** activation by P450 OleT$_{JE}$ enzymes, which indeed is what has been observed experimentally [36]. Interestingly, the reaction leading to hydroxylation products is considerably more exothermic than the one leading to desaturation by more than 50 kcal mol^{-1}. As such, the protein environment hampers OH rebound and affects the kinetics of the substrate activation process in favor of a much lesser exothermic pathway. This implies that P450 OleT$_{JE}$ reacts through negative catalysis, where an otherwise highly exothermic pathway is blocked in favor of a lesser exothermic reaction channel [85–87].

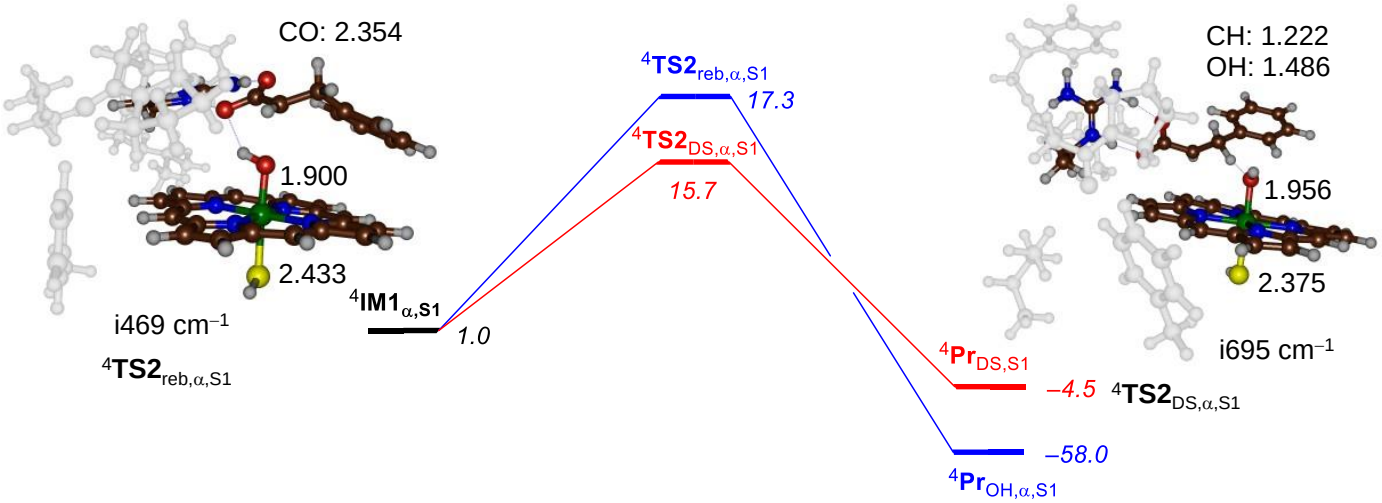

Figure 4. Substrate desaturation and hydroxylation bifurcation pathways for substrate **S1** from the radical intermediate **IM1**$_{\alpha,S1}$ of P450 OleT$_{JE}$. The middle panel gives energies relative to ^{4}**Re**$_{S1}$ in kcal mol^{-1} as obtained at the ΔE+ZPE level of theory. Transition state structures are shown on the side with bond lengths in angstroms and the imaginary frequency in the transition state in cm^{-1}.

The transition states have typical features of OH rebound and desaturation barriers and match previous work on substrate hydroxylation and desaturation by P450 enzymes [36,38,51–53,64–69,72,79,88,89]. The rebound transition state has a long C–O distance of 2.354 Å, although the imaginary frequency (i469 cm^{-1}) is clearly a pure C–O stretch vibration. As a matter of fact, a series of rebound calculations by biomimetic

iron(III)–hydroxo and manganese(III)–hydroxo complexes have similarly long C–O bonds in the transition states [90,91]. In the transition state, the Fe–O bond further elongates to 1.900 Å. In the desaturation transition state $\mathbf{TS2}_{DS,\alpha,S1}$, the same thing happens, and Fe–O elongates to 1.956 Å. Interestingly, the desaturation transition state is more reactant-like, with a shorter C–H (1.222 Å) than O–H (1.486 Å) distance.

Subsequently, we investigated the pathways from the alternative radical intermediate $\mathbf{IM1}_{\beta,S1}$ leading to desaturation, decarboxylation and β-hydroxylation. Figure 5 shows the potential energy profile for the pathways from $\mathbf{IM1}_{\beta,S1}$ leading to products and the various transition states that were characterized. The lowest energy barrier (of ΔE+ZPE = 4.3 kcal mol^{-1} above $\mathbf{IM1}_{\beta,S1}$) involves a second hydrogen atom abstraction and the formation of the desaturated products. At least 8.5 kcal mol^{-1} above the desaturation barrier is the OH rebound barrier $\mathbf{TS2}_{reb,\beta,S1}$, while the decarboxylation barrier is even higher (more than 20 kcal mol^{-1} above the desaturation barrier).

The rebound and desaturation barriers $\mathbf{TS2}_{reb,\beta,S1}$ and $\mathbf{TS2}_{DS,\beta,S1}$ are shown in Figure 5. In both structures, the Fe–O distance is long: 1.901 and 1.910 Å for $\mathbf{TS2}_{reb,\beta,S1}$ and $\mathbf{TS2}_{DS,\beta,S1}$, respectively, which matches the structures in Figure 4 well. The rebound C–O distance is even longer in $\mathbf{TS2}_{reb,\beta,S1}$ than in $\mathbf{TS2}_{reb,\alpha,S1}$ and is 2.679 Å. Nevertheless, the imaginary mode in the transition state (of i239 cm^{-1}) represents an O–C stretch vibration; hence, it is appropriate for a rebound barrier. Similar to $\mathbf{TS2}_{DS,\alpha,S1}$, $\mathbf{TS2}_{DS,\beta,S1}$ is also reactant-like, with a short C–O distance of 1.130 Å and a much longer O–H distance of 1.899 Å. Overall, these structures match previous barriers and landscapes calculated on analogous models but with different substrates.

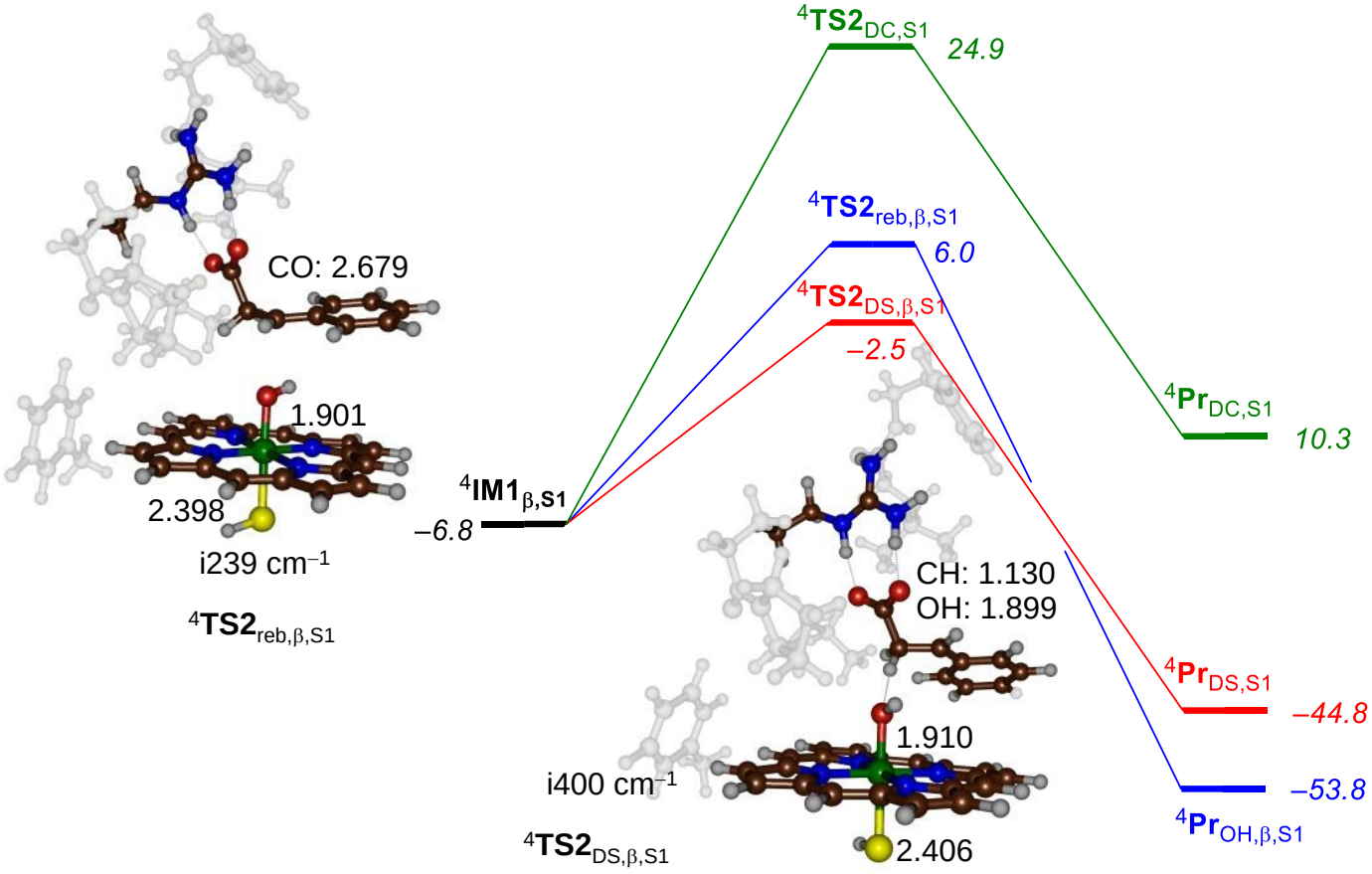

Figure 5. Substrate desaturation, decarboxylation and hydroxylation bifurcation pathways for substrate **S1** from the radical intermediate $\mathbf{IM1}_{\beta,S1}$ of P450 OleT$_{JE}$. The energy landscape gives energies relative to $^4\mathbf{Re}_{S1}$ in kcal mol^{-1} as obtained at the ΔE+ZPE level of theory. Transition state structures are shown with bond lengths in angstroms and the imaginary frequency in the transition state in cm^{-1}.

2.2. 2-Phenylbutyrate Activation by CpdI of P450 OleT$_{JE}$

To understand the effect of phenyl substitution to fatty acid substrates of P450 OleT$_{JE}$, we also investigated 2-phenylbutyrate activation by our CpdI model. For this particular system, we tested hydrogen atom abstraction pathways from the C$^{\alpha}$–H, C$^{\beta}$–H and C$^{\gamma}$–H positions; the obtained transition states and energy landscape for these three steps are shown in Figure 6. As it can be seen, the hydrogen atom abstraction barriers ^{4}**TS1**$_{HA,\alpha,S2}$ and ^{4}**TS1**$_{HA,\beta,S2}$ are within 1 kcal mol^{-1} in energy, although inclusion of entropy and thermal corrections appears to favor the C$^{\alpha}$–H pathway slightly. The C$^{\gamma}$–H hydrogen atom abstraction barrier, on the other hand, is well higher in energy (by ΔE+ZPE = 19.1 kcal mol^{-1}) than ^{4}**TS1**$_{HA,\beta,S2}$; consequently, this pathway is unlikely to happen, and we do not expect products originating from C$^{\gamma}$–H hydrogen atom abstraction.

The optimized geometries of ^{4}**TS1**$_{HA,\alpha,S2}$, ^{4}**TS1**$_{HA,\beta,S2}$ and ^{4}**TS1**$_{HA,\gamma,S2}$ are presented alongside the landscape in Figure 6. All three structures have their Fe–S distances in the window from 2.393 to 2.494 Å, while the Fe–O distance ranges from 1.725 for ^{4}**TS1**$_{HA,\alpha,S2}$ to 1.790 Å for ^{4}**TS1**$_{HA,\beta,S2}$. All three transition states are product-like, with shorter O–H than C–H distances. Moreover, they are all characterized with a large imaginary frequency that implies a significant amount of tunneling will take place and probably the kinetics will be affected by isotopic substitution of hydrogen atoms by deuterium in the substrate.

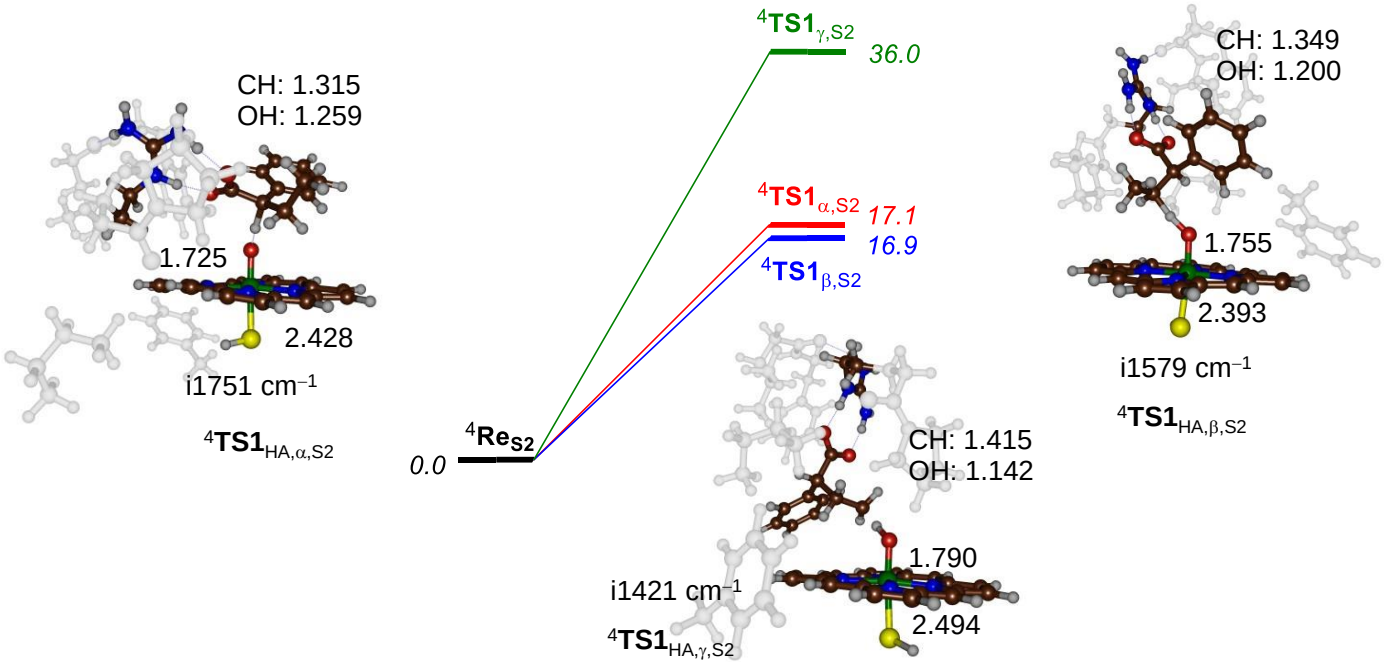

Figure 6. Hydrogen atom abstraction steps from substrate **S2** by CpdI of P450 OleT$_{JE}$. The middle panel gives relative energies in kcal mol^{-1} as obtained at the ΔE+ZPE level of theory. Hydrogen atom abstraction transition state structures are shown on the side with bond lengths in angstroms and the imaginary frequency in the transition state in cm^{-1}.

Next, we investigated the bifurcation pathways from each of the radical intermediates ^{4}**IM1**$_{\alpha,S2}$, ^{4}**IM1**$_{\beta,S2}$ and ^{4}**IM1**$_{\gamma,S2}$. The energy landscape for the product formation step from ^{4}**IM1**$_{\alpha,S2}$ is shown in Figure 7, and two possibilities were considered, namely, OH rebound to form the C$^{\alpha}$ alcohol or desaturation of the C$^{\alpha}$–C$^{\beta}$ bond. The lowest energy pathway is the rebound step with a barrier of about 8.6 kcal mol^{-1} above ^{4}**IM1**$_{\alpha,S2}$. This is a significant barrier as usually rebound barriers are much smaller in energy and typically have a magnitude between 0 and 4 kcal mol^{-1} [79,91]. Clearly, the protein environment and hydrogen bonding interactions restrict the OH rebound and hamper and slow this process down. Nevertheless, our prediction that the products originating from ^{4}**IM1**$_{\alpha,S2}$ should give α-hydroxylation matches experimental observations excellently as those were the dominant products obtained for this substrate in reaction with P450 OleT$_{JE}$ [36].

The rebound transition state is similar in structure to the one shown above in Figure 4, with a long C^{α}–O distance of 2.469 Å and a small imaginary frequency of i255 cm^{-1} representing the C^{α}–O stretch vibration. In agreement with the rebound transition states mentioned above, the Fe–O distance has elongated and is 1.898 Å in ^{4}**TS2**$_{reb,\alpha,S2}$, whereas the Fe–S distance is 2.433 Å. We also attempted to locate the transition state for the second hydrogen atom abstraction from ^{4}**IM1**$_{\alpha,S2}$; however, the barrier is relatively high in energy, i.e., well above that for ^{4}**TS2**$_{reb,\alpha,S2}$, and an estimate from the geometry scan located it 15.8 kcal mol^{-1} above the radical intermediate. Consequently, we do not expect desaturation products to appear after C^{α}–H hydrogen atom abstraction, and this channel will give dominant C^{α} hydroxylation products only.

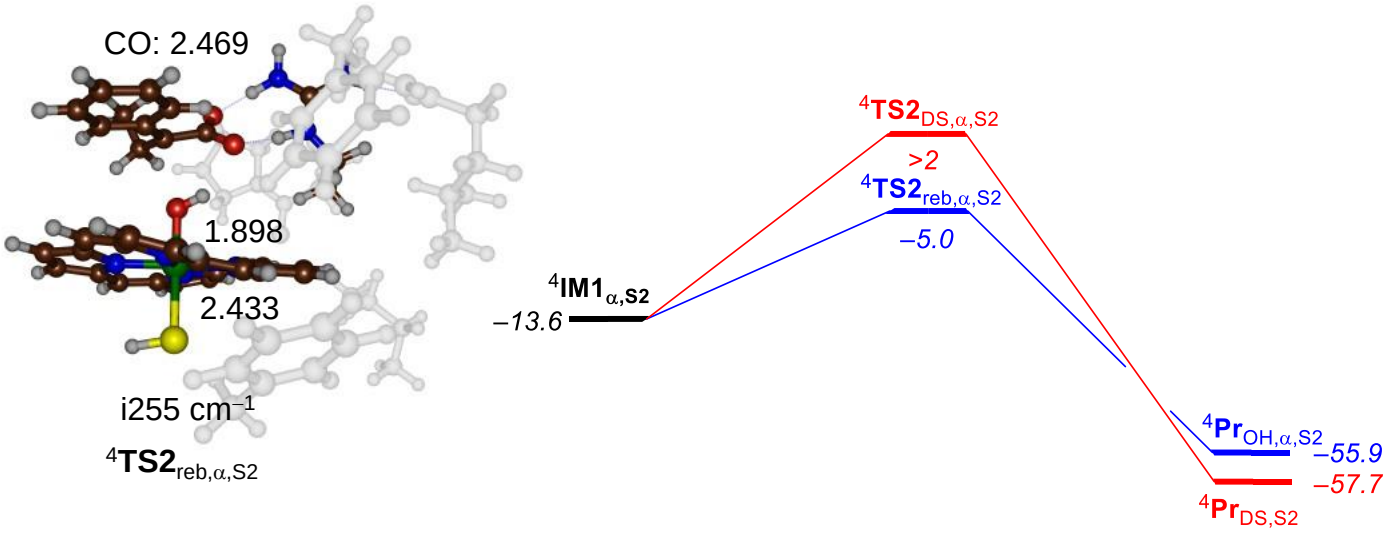

Figure 7. Substrate desaturation and hydroxylation bifurcation pathways for substrate **S2** from the radical intermediate **IM1**$_{\alpha,S2}$ of P450 $OleT_{JE}$. The right-hand side shows energies relative to ^{4}**Re**$_{S2}$ in kcal mol^{-1} as obtained at the ΔE+ZPE level of theory. The rebound transition state structure is shown on the left with bond lengths in angstroms and the imaginary frequency in the transition state in cm^{-1}. The desaturation transition state energy was estimated from constraint geometry scans.

The energy landscapes for the bifurcation pathways from ^{4}**IM1**$_{\beta,S2}$ are displayed in Figure 8. The lowest energy pathway is the second hydrogen atom abstraction leading to desaturation of the C^{α}–C^{β} bond, with a barrier of ΔE+ZPE = 3.1 kcal mol^{-1} above the radical intermediate. The alternative decarboxylation mechanism, however, is high in energy and well higher by 15.3 kcal mol^{-1} and, consequently, will have a very minor role of importance for this substrate. Indeed, experimental studies on this particular system did not record any product originating from decarboxylation of the substrate, which is consistent with the results shown here. Optimized geometries of the two bifurcation transition states ^{4}**TS2**$_{DS,\beta,S2}$ and ^{4}**TS2**$_{DC,\beta,S2}$ are also shown in Figure 8. In both cases, the Fe–O distance has elongated with respect to the reactant complex, and it is 1.916 Å for ^{4}**TS2**$_{DS,\beta,S2}$ and 1.803 Å for ^{4}**TS2**$_{DC,\beta,S2}$. The carboxylation takes place at a long C–C^{α} distance of 2.285 Å but has a clear C–C stretch vibration as an imaginary frequency with a magnitude of i291 cm^{-1}. A similar size imaginary frequency of i330 cm^{-1} for the desaturation barrier was recorded. This value is very small for a hydrogen atom abstraction transition state and well lower than the **TS1** transition states shown above in Figures 3 and 6. Consequently, the second hydrogen atom abstraction will not be affected from the same major kinetic isotope effects as the **TS1** barriers reported above and limited quantum mechanical tunneling will incur during the **TS2**$_{DS}$ transition. The desaturation transition state is highly reactant-like and early, with a short C–H distance of 1.163 Å and a very long O–H distance of 1.772 Å.

Overall, the calculations performed on S2 activation by our P450 $OleT_{JE}$ models show competitive reaction channels originating from C^{α}–H and C^{β}–H hydrogen atom abstraction. However, the former channel leads to dominant C^{α} hydroxylation products, whereas the latter channel gives desaturation instead. As such, the calculations predict a mixture of products. This is in good agreement with the product distributions reported by Pickl et al. [36] that gave a ratio of 332:80 for C^{α} hydroxylation versus desaturation of 2-phenylbutyrate by P450 $OleT_{JE}$. To understand the differences in product distributions obtained for S1 and S2 substrates, we analyzed the electronic properties of the various structures and investigated C–H bond strengths of the substrates.

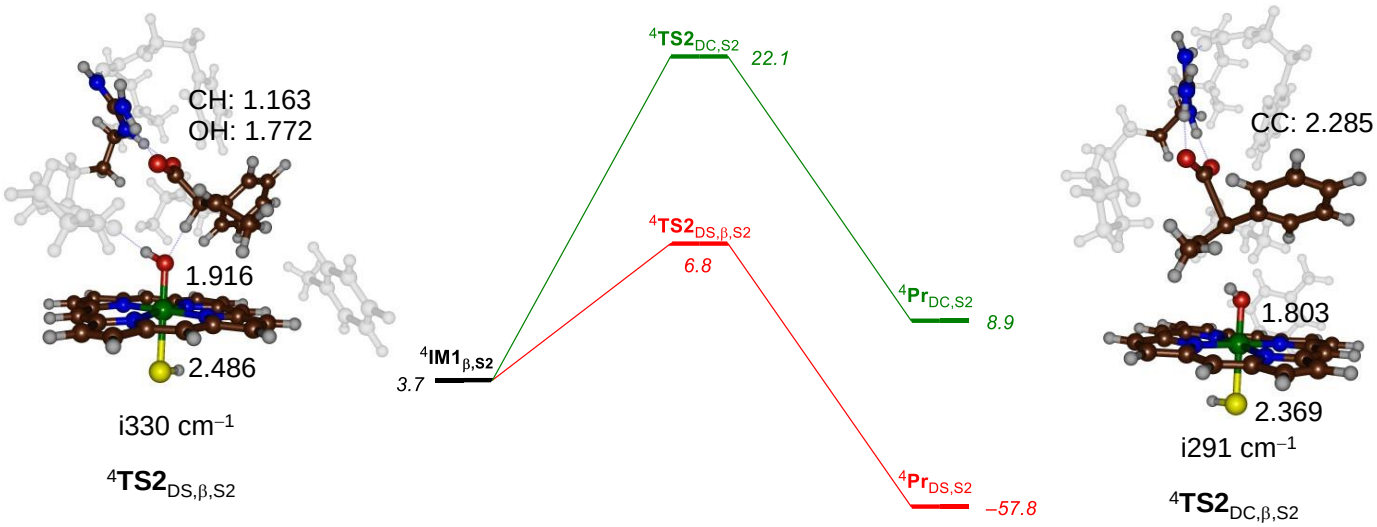

Figure 8. Substrate desaturation and decarboxylation bifurcation pathways for substrate **S2** from the radical intermediate $\mathbf{IM1}_{\beta,S2}$ of P450 $OleT_{JE}$. The energy landscape gives energies relative to $^4\mathbf{Re}_{S2}$ in kcal mol^{-1} as obtained at the ΔE+ZPE level of theory. Transition state structures are shown with bond lengths in angstroms and the imaginary frequency in the transition state in cm^{-1}.

3. Discussion

This work studies substrate activation by P450 $OleT_{JE}$ enzymes. In particular, the substrates 3-phenylpropionate (**S1**) and 2-phenylbutyrate (**S2**) and the pathways leading to α-hydroxylation, β-hydroxylation, desaturation and decarboxylation were investigated. DFT cluster models of the enzyme mechanism show that the reaction is stepwise via a radical intermediate and proceeds with a rate-determining hydrogen atom abstraction step. The absolute energies of the barriers are quite different for the two substrates, whereby for **S1**, the lowest barrier is for C^{β}–H hydrogen atom abstraction (ΔE+ZPE = 14.6 kcal mol^{-1}), while the C^{α}–H barrier is well higher (ΔE+ZPE = 20.9 kcal mol^{-1}). By contrast, for substrate **S2**, the two barriers are within 0.2 kcal mol^{-1} with a small preference of the C^{β}–H channel. As such, a mixture of products is expected for **S2**. In particular, for substrate **S2**, the C^{α}–H hydrogen atom abstraction is followed by a low-energy OH rebound barrier to give α-hydroxylation, whereas the C^{β}–H hydrogen atom abstraction leads to desaturation with a subsequent second hydrogen atom abstraction. These predicted products, i.e., α-hydroxylation and desaturation, for substrate **S2** activation by P450 $OleT_{JE}$ are in perfect agreement with the product distributions reported by Pickl et al. [36].

To understand the difference in hydrogen atom abstraction barriers between the two substrates, we calculated C–H bond dissociation energies (BDEs) for isolated substrates in the gas phase at the B3LYP/6-311++G** level of theory (with a solvent model included). These BDEs were calculated from the adiabatic homolytic bond strengths as the difference in energy (ΔE+ZPE) of the substrate, a hydrogen atom and the substrate with a hydrogen atom removed. Previously, we showed that hydrogen atom abstraction barriers often correlate with the BDE of the substrate C–H bond that is broken [92–94], Figure 9. For

substrate **S1**, the C^{α}–H bond has a $BDE_{CH,\,S1,\alpha}$ = 88.4 kcal mol^{-1}, while the C^{β}–H bond has a strength of 80.8 kcal mol^{-1}. As such, the C^{β}–H bond is the weakest bond in the substrate and the most likely bond to be activated by the enzyme. Indeed, our potential energy landscape (Figure 3) for **S1** activation by P450 $OleT_{JE}$ gives a lower hydrogen atom abstraction barrier for C^{β}–H than for C^{α}–H, in line with the differences in the bond strengths of the two bonds in the substrate. Clearly, the protein pocket does not affect the selectivity of the reaction, and P450 $OleT_{JE}$ appears to abstract the weakest C–H bond of the substrate.

We also calculated the C^{α}–H, C^{β}–H and C^{γ}–H bond strengths of substrate **S2** (see Figure 9). Not surprisingly, the weakest bond is the tertiary C^{α}–H bond with a BDE = 78.0 kcal mol^{-1}. Much stronger are the C^{β}–H bond (BDE = 91.0 kcal mol^{-1}) and C^{γ}–H (95.8 kcal mol^{-1}). Indeed, our DFT-calculated energy landscape for hydrogen atom abstraction from these three positions returns a high energy barrier for C^{γ}–H abstraction of ΔE+ZPE = 36.0 kcal mol^{-1}, and hence we do not expect this reaction channel to occur. Interestingly, despite the fact that the BDEs for C^{α}–H and C^{β}–H are widely apart, P450 $OleT_{JE}$ appears to be able to activate both positions, and we find almost equal hydrogen atom abstraction barriers for these pathways. Therefore, the second coordination sphere and substrate binding and positioning affect the chemoselectivity of the reaction and make the C^{β}–H abstraction accessible. This is a form of negative catalysis [85–87] and means an otherwise high-energy reaction channel is stabilized by the protein environment and makes alternative products possible. In particular, the approach of the C^{α}–H bond of **S2** on CpdI is sterically hindered through protein residues, meaning that this position is less accessible than the C^{β}–H position of the substrate. The shape of the substrate binding pocket, therefore, guides the regioselectivity and the accessibility to the substrate and overrules thermochemical preferences such as the C–H bond strength.

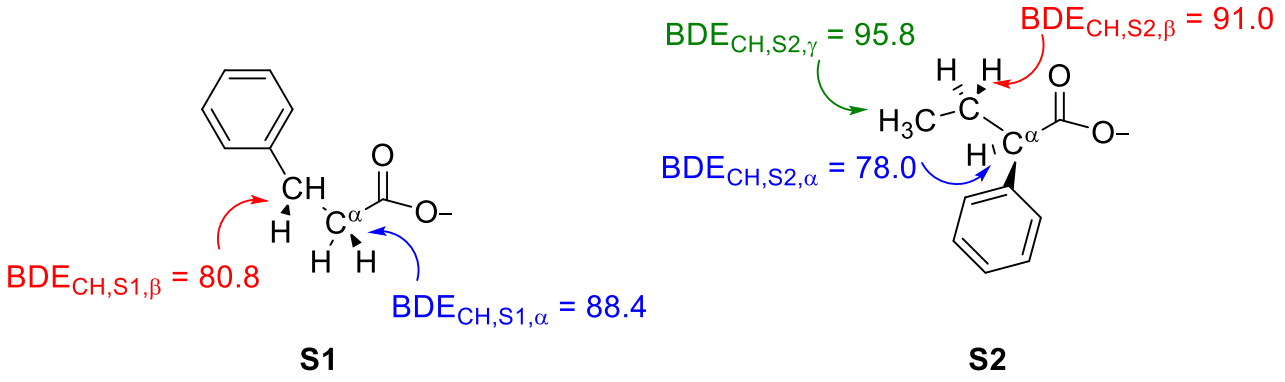

Figure 9. Calculated substrate BDE values for selected C–H bonds in **S1** and **S2**. Values are ΔE+ZPE in kcal mol^{-1}.

4. Materials and Methods

We used density functional theory (DFT) methods as implemented in the *Gaussian*-09 software package [95]. The studies used the unrestricted hybrid density functional method B3LYP [96,97] for all calculations. The initial geometry optimizations, constraint geometry scans and analytical frequency calculations used a modest LACVP basis set on iron (with core potential) [98] coupled to 6-31G on the rest of the atoms: basis set BS1 [99]. All calculations were run with a solvent model included through the continuous polarized continuum model with a dielectric constant representing chlorobenzene (with dielectric constant ε = 5.7) [100]. The quality of the energies was improved through single point calculations with a 6-311+G* basis set on all atoms and LACV3P+ with core potential on iron: basis set BS2. Our methods have been extensively validated and benchmarked against experimental data, and these procedures were shown to reproduce experimental product distributions and rate constants well [101–104]. Full data of all results obtained is given in the Supporting Information accompanying this paper (Supplementary Materials).

5. Conclusions

In this work, a computational study into the activation of 3-phenylpropionate and 2-phenylbutyrate by Compound I of P450 $OleT_{JE}$ was conducted. We set up large active site cluster models of well over 150 atoms that contain the heme and its direct ligands, the substrate and key residues in the substrate binding pocket. We then studied all mechanisms leading to C^{α} hydroxylation, C^{β} hydroxylation, C^{γ} hydroxylation, C^{α}–C^{β} desaturation and decarboxylation. We showed that differences in the size and shape of the substrate give differences in orientation and, consequently, different product distributions. Thus, for 3-phenylpropionate, dominant desaturation products were produced through a rate-determining C^{β}–H hydrogen atom abstraction channel. By contrast, 2-phenylbutyrate has competing hydrogen atom abstraction barriers for C^{α}–H and C^{β}–H abstractions and therefore gives a mixture of C^{α} hydroxylation and desaturation pathways. These predicted products are in excellent agreement with those reported previously from experimental studies on the same enzyme. The barrier heights were rationalized by comparing them to the C–H bond strengths in the substrate, and the effect of substrate binding and the second coordination sphere was discussed.

Supplementary Materials: The following are available online at https://www.mdpi.com/article/10.3390/ijms22137172/s1.

Author Contributions: Conceptualization, S.P.d.V.; data curation, Y.-T.L.; writing—original draft preparation, S.P.d.V. Both authors have read and agreed to the published version of the manuscript.

Funding: This research received no external funding.

Institutional Review Board Statement: Not applicable.

Informed Consent Statement: Not applicable.

Data Availability Statement: Data available in a publicly accessible repository.

Acknowledgments: The Computational Shared Facilities of the University of Manchester is acknowledged for providing computational resources for this study.

Conflicts of Interest: The authors declare no conflict of interest.

References

1. Beeson, W.T.; Vu, V.V.; Span, E.A.; Phillips, C.M.; Marletta, M.A. Cellulose degradation by polysaccharide monooxygenases. *Ann. Rev. Biochem.* **2015**, *84*, 923–946. [CrossRef]
2. Kang, A.; Lee, T.S. Converting sugars to biofuels: Ethanol and beyond. *Bioengineering* **2015**, *2*, 184–203. [CrossRef] [PubMed]
3. Walton, P.H.; Davies, G.J. On the catalytic mechanisms of lytic polysaccharide monooxygenases. *Curr. Opin. Chem. Biol.* **2016**, *31*, 195–207. [CrossRef]
4. Lup, A.N.K.; Abnisa, F.; Daud, W.M.A.W.; Aroua, M.K. A review on reaction mechanisms of metal-catalyzed deoxygenation process in bio-oil model compounds. *Appl. Catal. A* **2017**, *541*, 87–106. [CrossRef]
5. Coines, J.; Raich, L.; Rovira, C. Modeling catalytic reaction mechanisms in glycoside hydrolases. *Curr. Opin. Chem. Biol.* **2019**, *53*, 183–191. [CrossRef] [PubMed]
6. Mendoza, F.; Masgrau, L. Computational modeling of carbohydrate processing enzymes reactions. *Curr. Opin. Chem. Biol.* **2021**, *61*, 203–213. [CrossRef] [PubMed]
7. Jarvis, A.G. Designer metalloenzymes for synthetic biology: Enzyme hybrids for catalysis. *Curr. Opin. Chem. Biol.* **2020**, *58*, 63–71. [CrossRef]
8. Das, A.; Hessin, C.; Ren, Y.; Desage-El Murr, M. Biological concepts for catalysis and reactivity: Empowering bioinspiration. *Chem. Soc. Rev.* **2020**, *49*, 8840–8867. [CrossRef]
9. Ghosh, A.C.; Duboc, C.; Gennari, M. Synergy between metals for small molecule activation: Enzymes and bioinspired complexes. *Coord. Chem. Rev.* **2021**, *428*, 213606. [CrossRef]
10. Sono, M.; Roach, M.P.; Coulter, E.D.; Dawson, J.H. Heme-containing oxygenases. *Chem. Rev.* **1996**, *96*, 2841–2888. [CrossRef]
11. Meunier, B.; de Visser, S.P.; Shaik, S. Mechanism of oxidation reactions catalyzed by cytochrome P450 enzymes. *Chem. Rev.* **2004**, *104*, 3947–3980. [CrossRef]
12. Denisov, I.G.; Makris, T.M.; Sligar, S.G.; Schlichting, I. Structure and chemistry of cytochrome P450. *Chem. Rev.* **2005**, *105*, 2253–2277. [CrossRef] [PubMed]
13. Ortiz de Montellano, P.R. (Ed.) *Cytochrome P450: Structure, Mechanism and Biochemistry*, 3rd ed.; Kluwer Academic/Plenum Publishers: New York, NY, USA, 2005.

14. Kadish, K.M.; Smith, K.M.; Guilard, R. (Eds.) *Handbook of Porphyrin Science*; World Scientific Publishing Co.: Hackensack, NJ, USA, 2010.
15. Grogan, G. Cytochromes P450: Exploiting diversity and enabling application as biocatalysts. *Curr. Opin. Chem. Biol.* **2011**, *15*, 241–248. [CrossRef] [PubMed]
16. Fasan, R. Tuning P450 enzymes as oxidation catalysts. *ACS Catal.* **2012**, *2*, 647–666. [CrossRef]
17. Poulos, T.L. Heme enzyme structure and function. *Chem. Rev.* **2014**, *114*, 3919–3962. [CrossRef]
18. Huang, X.; Groves, J.T. Oxygen activation and radical transformations in heme proteins and metalloporphyrins. *Chem. Rev.* **2018**, *118*, 2491–2553. [CrossRef] [PubMed]
19. Schofield, C.J.; Zhang, Z. Structural and mechanistic studies on 2-oxoglutarate-dependent oxygenases and related enzymes. *Curr. Opin. Struc. Biol.* **1999**, *9*, 722–731. [CrossRef]
20. Solomon, E.I.; Brunold, T.C.; Davis, M.I.; Kemsley, J.N.; Lee, S.K.; Lehnert, N.; Neese, F.; Skulan, A.J.; Yang, Y.S.; Zhou, J. Geometric and electronic structure/function correlations in non-heme iron enzymes. *Chem. Rev.* **2000**, *100*, 235–349. [CrossRef] [PubMed]
21. Abu-Omar, M.M.; Loaiza, A.; Hontzeas, N. Reaction mechanisms of mononuclear non-heme iron oxygenases. *Chem. Rev.* **2005**, *105*, 2227–2252. [CrossRef]
22. Krebs, C.; Galonić Fujimori, D.; Walsh, C.T.; Bollinger Jr, J.M. Non-heme Fe(IV)–oxo intermediates. *Acc. Chem. Res.* **2007**, *40*, 484–492. [CrossRef]
23. Kovaleva, E.G.; Lipscomb, J.D. Versatility of biological non-heme Fe(II) centers in oxygen activation reactions. *Nat. Chem. Biol.* **2008**, *4*, 186–193. [CrossRef] [PubMed]
24. de Visser, S.P.; Kumar, D. (Eds.) *Iron-Containing Enzymes: Versatile Catalysts of Hydroxylation Reactions in Nature*; Royal Society of Chemistry Publishing: Cambridge, UK, 2011.
25. White, M.D.; Flashman, E. Catalytic strategies of the non-heme iron dependent oxygenases and their roles in plant biology. *Curr. Opin. Chem. Biol.* **2016**, *31*, 126–135. [CrossRef]
26. De Visser, S.P. Mechanistic insight on the activity and substrate selectivity of nonheme iron dioxygenases. *Chem. Rec.* **2018**, *18*, 1501–1516. [CrossRef]
27. Shoji, O.; Fujishiro, T.; Nakajima, H.; Kim, M.; Nagano, S.; Shiro, Y.; Watanabe, Y. Hydrogen peroxide dependent monooxygenations by tricking the substrate recognition of cytochrome $P450_{BS\beta}$. *Angew. Chem. Int. Ed.* **2007**, *46*, 3656–3659. [CrossRef]
28. Rude, M.A.; Baron, T.S.; Brubaker, S.; Alibhai, M.; Del Cardayre, S.B.; Schirmer, A. Terminal olefin (1-alkene) biosynthesis by a novel P450 fatty acid decarboxylase from *Jeotgalicoccus* Species. *Appl. Environ. Microbiol.* **2011**, *77*, 1718–1727. [CrossRef] [PubMed]
29. Liu, Y.; Wang, C.; Yan, J.; Zhang, W.; Guan, W.; Lu, X.; Li, S. Hydrogen peroxide-independent production of α-alkenes by $OleT_{JE}$ P450 fatty acid decarboxylase. *Biotechnol. Biofuels* **2014**, *7*, 28–40. [CrossRef]
30. Shoji, O.; Watanabe, Y. Peroxygenase reactions catalyzed by cytochromes P450. *J. Biol. Inorg. Chem.* **2014**, *19*, 529–539. [CrossRef]
31. Dennig, A.; Kuhn, M.; Tassoti, S.; Thiessenhusen, A.; Gilch, S.; Bülter, T.; Haas, T.; Hall, M.; Faber, K. Oxidative decarboxylation of short-chain fatty acids to 1-alkenes. *Angew. Chem. Int. Ed.* **2015**, *54*, 8819–8822. [CrossRef] [PubMed]
32. Grant, J.L.; Hsieh, C.H.; Makris, T.M. Decarboxylation of fatty acids to terminal alkenes by cytochrome P450 Compound I. *J. Am. Chem. Soc.* **2015**, *137*, 4940–4943. [CrossRef]
33. Grant, J.L.; Mitchell, M.E.; Makris, T.M. Catalytic strategy for carbon−carbon bond scission by the cytochrome P450 OleT. *Proc. Natl. Acad. Sci. USA* **2016**, *113*, 10049–10054. [CrossRef] [PubMed]
34. Wang, Y.; Lan, D.; Durrani, R.; Hollmann, F. Peroxygenases en route to becoming dream catalysts. What are the opportunities and challenges? *Curr. Opin. Chem. Biol.* **2017**, *37*, 1–9. [CrossRef]
35. Munro, A.W.; McLean, K.J.; Grant, J.L.; Makris, T.M. Structure and function of the cytochrome P450 peroxygenase enzymes. *Biochem. Soc. Trans.* **2018**, *46*, 183–196. [CrossRef]
36. Pickl, M.; Kurakin, S.; Cantú Reinhard, F.G.; Schmid, P.; Pöcheim, A.; Winkler, C.K.; Kroutil, W.; de Visser, S.P.; Faber, K. Mechanistic studies of fatty acid activation by CYP152 peroxygenases reveal unexpected desaturase activity. *ACS Catal.* **2019**, *9*, 565–577. [CrossRef]
37. Bauer, D.; Zachos, I.; Sieber, V. Production of propene from n-butanol: A three-step cascade utilizing the cytochrome P450 fatty acid decarboxylase $OleT_{JE}$. *ChemBioChem* **2020**, *21*, 3273–3281. [CrossRef] [PubMed]
38. Chowdhury, A.S.; Ali, H.S.; Faponle, A.S.; de Visser, S.P. How external perturbations affect the chemoselectivity of substrate activation by cytochrome P450 $OleT_{JE}$. *Phys. Chem. Chem. Phys.* **2020**, *22*, 27178–27190. [CrossRef]
39. Derat, E.; Shaik, S. The Poulos-Kraut mechanism of Compound I formation in horseradish peroxidase: A QM/MM study. *J. Phys. Chem. B* **2006**, *110*, 10526–10533. [CrossRef]
40. Cho, K.-B.; Derat, E.; Shaik, S. Compound I of nitric oxide synthase: The active site protonation state. *J. Am. Chem. Soc.* **2007**, *129*, 3182–3188. [CrossRef] [PubMed]
41. de Visser, S.P.; Tan, L.S. Is the bound substrate in nitric oxide synthase protonated or neutral and what is the active oxidant that performs substrate hydroxylation? *J. Am. Chem. Soc.* **2008**, *130*, 12961–12974. [CrossRef]
42. Vidossich, P.; Fiorin, G.; Alfonso-Prieto, M.; Derat, E.; Shaik, S.; Rovira, C. On the role of water in peroxidase catalysis: A theoretical investigation of HRP Compound I formation. *J. Phys. Chem. B* **2010**, *114*, 5161–5169. [CrossRef] [PubMed]
43. Li, X.-X.; Postils, V.; Sun, W.; Faponle, A.S.; Solà, M.; Wang, Y.; Nam, W.; de Visser, S.P. Reactivity patterns of (protonated) Compound II and Compound I of Cytochrome P450: Which is the better oxidant? *Chem. Eur. J.* **2017**, *23*, 6406–6418. [CrossRef]

44. Faponle, A.S.; Seebeck, F.P.; de Visser, S.P. Sulfoxide synthase versus cysteine dioxygenase reactivity in a nonheme iron enzyme. *J. Am. Chem. Soc.* **2017**, *139*, 9259–9270. [CrossRef] [PubMed]
45. Timmins, A.; Saint-André, M.; de Visser, S.P. Understanding how prolyl-4-hydroxylase structure steers a ferryl oxidant toward scission of a strong C–H bond. *J. Am. Chem. Soc.* **2017**, *139*, 9855–9866. [CrossRef] [PubMed]
46. Lin, Y.-T.; Ali, H.S.; de Visser, S.P. Electrostatic perturbations from the protein affect C–H bond strengths of the substrate and enable negative catalysis in the TmpA biosynthesis enzyme. *Chem. Eur. J.* **2021**, *27*, 8851–8864. [CrossRef] [PubMed]
47. Belcher, J.; McLean, K.J.; Matthews, S.; Woodward, L.S.; Fisher, K.; Rigby, S.E.J.; Nelson, D.R.; Potts, D.; Baynham, M.T.; Parker, D.A.; et al. Structure and biochemical properties of the alkene producing cytochrome P450 $OleT_{JE}$ (CYP152L1) from the *Jeotgalicoccus* sp. 8456 bacterium. *J. Biol. Chem.* **2014**, *289*, 6535–6550. [CrossRef]
48. Berman, H.M.; Westbrook, J.; Feng, Z.; Gilliland, G.; Bhat, T.N.; Weissig, H.; Shindyalov, I.N.; Bourne, P.E. The protein databank. *Nucl. Acids Res.* **2000**, *28*, 235–243. [CrossRef]
49. Quesne, M.G.; Borowski, T.; de Visser, S.P. Quantum mechanics/molecular mechanics modelling of enzymatic processes: Caveats and breakthroughs. *Chem. Eur. J.* **2016**, *22*, 2562–2581. [CrossRef]
50. Mubarak, M.Q.E.; Gérard, E.F.; Blanford, C.F.; Hay, S.; de Visser, S.P. How do vanadium chloroperoxidases generate hypochlorite from hydrogen peroxide and chloride? A computational study. *ACS Catal.* **2020**, *10*, 14067–14079. [CrossRef]
51. Ji, L.; Faponle, A.S.; Quesne, M.G.; Sainna, M.A.; Zhang, J.; Franke, A.; Kumar, D.; van Eldik, R.; Liu, W.; de Visser, S.P. Drug metabolism by cytochrome P450 enzymes: What distinguishes the pathways leading to substrate hydroxylation over desaturation? *Chem. Eur. J.* **2015**, *21*, 9083–9092. [CrossRef]
52. Faponle, A.S.; Quesne, M.G.; de Visser, S.P. Origin of the regioselective fatty acid hydroxylation versus decarboxylation by a cytochrome P450 peroxygenase: What drives the reaction to biofuel production? *Chem. Eur. J.* **2016**, *22*, 5478–5483. [CrossRef]
53. Cantú Reinhard, F.G.; Lin, Y.-T.; Stańczak, A.; de Visser, S.P. Bioengineering of cytochrome P450 $OleT_{JE}$: How does substrate positioning affect the product distributions? *Molecules* **2020**, *25*, 2675–2697. [CrossRef]
54. Green, M.T. Evidence for sulfur-based radicals in thiolate compound I intermediates. *J. Am. Chem. Soc.* **1999**, *121*, 7939–7940. [CrossRef]
55. Ogliaro, F.; Cohen, S.; de Visser, S.P.; Shaik, S. Medium polarization and hydrogen bonding effects on Compound I of cytochrome P450: What kind of a radical is it really? *J. Am. Chem. Soc.* **2000**, *122*, 12892–12893. [CrossRef]
56. Ogliaro, F.; de Visser, S.P.; Cohen, S.; Kaneti, J.; Shaik, S. The experimentally elusive oxidant of cytochrome P450: A theoretical "trapping" defining more closely the "real" species. *ChemBioChem* **2001**, *2*, 848–851. [CrossRef]
57. de Visser, S.P.; Shaik, S.; Sharma, P.K.; Kumar, D.; Thiel, W. Active species of horseradish peroxidase (HRP) and cytochrome P450: Two electronic chameleons. *J. Am. Chem. Soc.* **2003**, *125*, 15779–15788. [CrossRef] [PubMed]
58. Hersleth, H.-P.; Ryde, U.; Rydberg, P.; Görbitz, C.H.; Andersson, K.K. Structures of the high-valent metal-ion haem–oxygen intermediates in peroxidases, oxygenases and catalases. *J. Inorg. Biochem.* **2006**, *100*, 460–476. [CrossRef] [PubMed]
59. Groenhof, A.R.; Ehlers, A.W.; Lammertsma, K. Proton assisted oxygen-oxygen bond splitting in cytochrome P450. *J. Am. Chem. Soc.* **2007**, *129*, 6204–6209. [CrossRef]
60. Bathelt, C.M.; Zurek, J.; Mulholland, A.J.; Harvey, J.N. Electronic structure of compound I in human isoforms of cytochrome P450 from QM/MM modeling. *J. Am. Chem. Soc.* **2005**, *127*, 12900–12908. [CrossRef]
61. Shaik, S.; Kumar, D.; de Visser, S.P.; Altun, A.; Thiel, W. Theoretical perspective on the structure and mechanism of cytochrome P450 enzymes. *Chem. Rev.* **2005**, *105*, 2279–2328. [CrossRef]
62. Rydberg, P.; Sigfridsson, E.; Ryde, U. On the role of the axial ligand in heme proteins: A theoretical study. *J. Biol. Inorg. Chem.* **2004**, *9*, 203–223. [CrossRef]
63. Harvey, J.N.; Bathelt, C.M.; Mulholland, A.J. QM/MM modeling of compound I active species in cytochrome P450, cytochrome c peroxidase, and ascorbate peroxidase. *J. Comput. Chem.* **2006**, *27*, 1352–1362. [CrossRef]
64. Li, D.; Wang, Y.; Han, K.; Zhan, C.-G. Fundamental reaction pathways for cytochrome P450-catalyzed 5′-hydroxylation and N-demethylation of nicotine. *J. Phys. Chem. B* **2010**, *114*, 9023–9030. [CrossRef]
65. Hirao, H.; Chuanprasit, P.; Cheong, Y.Y.; Wang, X. How is a metabolic intermediate formed in the mechanism-based inactivation of cytochrome P450 by using 1,1-dimethylhydrazine: Hydrogen abstraction or nitrogen oxidation? *Chem. Eur. J.* **2013**, *19*, 7361–7369. [CrossRef]
66. Hirao, H.; Cheong, Z.C.; Wang, X. Pivotal role of water in terminating enzymatic function: A density functional theory study of the mechanism-based inactivation of cytochromes P450. *J. Phys. Chem. B* **2012**, *116*, 7787–7794. [CrossRef] [PubMed]
67. Lai, R.; Li, H. Hydrogen abstraction of camphor catalyzed by cytochrome $P450_{cam}$: A QM/MM study. *J. Phys. Chem. B* **2016**, *120*, 12312–12320. [CrossRef] [PubMed]
68. Wang, X.; Shi, J.; Liu, Y. Oxidative rearrangement mechanism of pentalenolactone F catalyzed by cytochrome P450 CYP161C2 (PntM). *Inorg. Chem.* **2018**, *57*, 8933–8941. [CrossRef]
69. Zhang, S.; Liu, Y. Mechanical insights into the enzymatic cleavage of double C–C bond in poly(cis-1,4-isoprene) by the latex clearing protein. *Inorg. Chem.* **2020**, *59*, 9627–9637. [CrossRef]
70. Phung, Q.M.; Pierloot, K. Low-lying electromeric states in chloro-ligated iron(IV)-oxo porphyrin as a model for compound I, studied with second-order perturbation theory based on density matrix renormalization group. *J. Chem. Theory Comput.* **2019**, *15*, 3033–3043. [CrossRef] [PubMed]

71. Altarsha, M.; Benighaus, T.; Kumar, D.; Thiel, W. How is the reactivity of cytochrome $P450_{cam}$ affected by Thr252X mutation? A QM/MM study for X = serine, valine, alanine, glycine. *J. Am. Chem. Soc.* **2009**, *131*, 4755–4763. [CrossRef]
72. Li, D.; Wang, Y.; Han, K. Recent density functional theory model calculations of drug metabolism by cytochrome P450. *Coord. Chem. Rev.* **2012**, *256*, 1137–1150. [CrossRef]
73. Sainna, M.A.; Kumar, S.; Kumar, D.; Fornarini, S.; Crestoni, M.E.; de Visser, S.P. A comprehensive test set of epoxidation rate constants by iron(IV)-oxo porphyrin complexes. *Chem. Sci.* **2015**, *6*, 1516–1529. [CrossRef] [PubMed]
74. Kepp, K.P. Heme isomers substantially affect heme's electronic structure and function. *Phys. Chem. Chem. Phys.* **2017**, *19*, 22355–22362. [CrossRef]
75. Kumar, D.; de Visser, S.P.; Shaik, S. Multistate reactivity in styrene epoxidation by Compound I of cytochrome P450: Mechanisms of products and side products formation. *Chem. Eur. J.* **2005**, *11*, 2825–2835. [CrossRef]
76. Kumar, D.; Karamzadeh, B.; Sastry, G.N.; de Visser, S.P. What factors influence the rate constant of substrate epoxidation by Compound I of cytochrome P450 and analogous iron(IV)-oxo oxidants. *J. Am. Chem. Soc.* **2010**, *132*, 7656–7667. [CrossRef]
77. Quesne, M.G.; Senthilnathan, D.; Singh, D.; Kumar, D.; Maldivi, P.; Sorokin, A.B.; de Visser, S.P. Origin of the enhanced reactivity of μ-nitrido-bridged diiron(IV)-oxo porphyrinoid complexes over cytochrome P450 Compound I. *ACS Catal.* **2016**, *6*, 2230–2243. [CrossRef]
78. Colomban, C.; Tobing, A.H.; Mukherjee, G.; Sastri, C.V.; Sorokin, A.B.; de Visser, S.P. Mechanism of oxidative activation of fluorinated aromatic compounds by N-bridged diiron-phthalocyanine. What determines the reactivity? *Chem. Eur. J.* **2019**, *25*, 14320–14331. [CrossRef]
79. Shaik, S.; Cohen, S.; de Visser, S.P.; Sharma, P.K.; Kumar, D.; Kozuch, S.; Ogliaro, F.; Danovich, D. The "rebound controversy": An overview and theoretical modeling of the rebound step in C–H hydroxylation by cytochrome P450. *Eur. J. Inorg. Chem.* **2004**, 207–226. [CrossRef]
80. Ali, H.S.; Henchman, R.H.; de Visser, S.P. Lignin biodegradation by a cytochrome P450 enzyme: A computational study into syringol activation by GcoA. *Chem. Eur. J.* **2020**, *26*, 13093–13102. [CrossRef]
81. de Visser, S.P.; Ogliaro, F.; Shaik, S. How does ethene inactivate cytochrome P450 en route to its epoxidation? A density functional study. *Angew. Chem. Int. Ed.* **2001**, *40*, 2871–2874. [CrossRef]
82. Kumar, D.; de Visser, S.P.; Shaik, S. How does product isotope effect prove the operation of a two-state "rebound" mechanism in C–H hydroxylation by cytochrome P450? *J. Am. Chem. Soc.* **2003**, *125*, 13024–13025. [CrossRef]
83. Kumar, D.; de Visser, S.P.; Sharma, P.K.; Cohen, S.; Shaik, S. Radical clock substrates, their C–H hydroxylation mechanism by cytochrome P450 and other reactivity patterns: What does theory reveal about the clocks' behavior? *J. Am. Chem. Soc.* **2004**, *126*, 1907–1920. [CrossRef]
84. Kumar, D.; de Visser, S.P.; Shaik, S. Oxygen economy of cytochrome P450: What is the origin of the mixed functionality as a dehydrogenase–oxidase enzyme compared with its normal function? *J. Am. Chem. Soc.* **2004**, *126*, 5072–5073. [CrossRef]
85. Rétey, J. Enzymic reaction selectivity by negative catalysis or how do enzymes deal with highly reactive intermediates? *Angew. Chem. Int. Ed.* **1990**, *29*, 355–361. [CrossRef]
86. Vögeli, B.; Erb, T.J. 'Negative' and 'positive catalysis': Complementary principles that shape the catalytic landscape of enzymes. *Curr. Opin. Chem. Biol.* **2018**, *47*, 94–100. [CrossRef] [PubMed]
87. de Visser, S.P.; Lin, Y.-T.; Ali, H.S.; Bagh, U.K.; Mukherjee, G.; Sastri, C.V. Negative catalysis or non-Bell-Evans-Polanyi reactivity by metalloenzymes: Examples from mononuclear heme and non-heme iron oxygenases. *Coord. Chem. Rev.* **2021**, *439*, 213914. [CrossRef]
88. Pangia, T.M.; Yadav, V.; Gérard, E.F.; Lin, Y.-T.; de Visser, S.P.; Jameson, G.N.L.; Goldberg, D.P. Mechanistic investigation of oxygen rebound in a mononuclear nonheme iron complex. *Inorg. Chem.* **2019**, *58*, 9557–9561. [CrossRef] [PubMed]
89. Cantú Reinhard, F.G.; de Visser, S.P. Oxygen atom transfer using an iron(IV)-oxo embedded in a tetracyclic N-heterocyclic carbene system: How does the reactivity compare to Cytochrome P450 Compound I? *Chem. Eur. J.* **2017**, *23*, 2935–2944. [CrossRef]
90. Cummins, D.C.; Alvarado, J.G.; Zaragoza, J.P.T.; Mubarak, M.Q.E.; Lin, Y.-T.; de Visser, S.P.; Goldberg, D.P. Hydroxyl transfer to carbon radicals by Mn(OH) versus Fe(OH) corrole complexes. *Inorg. Chem.* **2020**, *59*, 16053–16064. [CrossRef]
91. Codola, Z.; Gamba, I.; Acuña-Pares, F.; Casadevall, C.; Clemancey, M.; Latour, J.-M.; Luis, J.M.; Lloret-Fillol, J.; Costas, M. Design of iron coordination complexes as highly active homogenous water oxidation catalysts by deuteration of oxidation-sensitive sites. *J. Am. Chem. Soc.* **2019**, *141*, 323–333. [CrossRef] [PubMed]
92. de Visser, S.P.; Kumar, D.; Cohen, S.; Shacham, R.; Shaik, S. A predictive pattern of computed barriers for C–H hydroxylation by Compound I of cytochrome P450. *J. Am. Chem. Soc.* **2004**, *126*, 8362–8363. [CrossRef]
93. Shaik, S.; Kumar, D.; de Visser, S.P. A valence bond modeling of trends in hydrogen abstraction barriers and transition states of hydroxylation reactions catalyzed by cytochrome P450 enzymes. *J. Am. Chem. Soc.* **2008**, *130*, 10128–10140. [CrossRef] [PubMed]
94. Latifi, R.; Bagherzadeh, M.; de Visser, S.P. Origin of the correlation of the rate constant of substrate hydroxylation by nonheme iron(IV)-oxo complexes with the bond-dissociation energy of the C–H bond of the substrate. *Chem. Eur. J.* **2009**, *15*, 6651–6662. [CrossRef]
95. Frisch, M.J.; Trucks, G.W.; Schlegel, H.B.; Scuseria, G.E.; Robb, M.A.; Cheeseman, J.R.; Scalmani, G.; Barone, V.; Mennucci, B.; Petersson, G.A.; et al. *Gaussian 09, Revision D.01*; Gaussian, Inc.: Wallingford, CT, USA, 2013.
96. Becke, A.D. Density-functional thermochemistry. III. The role of exact exchange. *J. Chem. Phys.* **1993**, *98*, 5648–5652. [CrossRef]

97. Lee, C.; Yang, W.; Parr, R.G. Development of the Colle-Salvetti correlation-energy formula into a functional of the electron density. *Phys. Rev. B* **1988**, *37*, 785–789. [CrossRef] [PubMed]
98. Hay, P.J.; Wadt, W.R. Ab initio effective core potentials for molecular calculations. Potentials for the transition metal atoms Sc to Hg. *J. Chem. Phys.* **1985**, *82*, 270–272. [CrossRef]
99. Hehre, W.J.; Ditchfield, R.; Pople, J.A. Self—consistent molecular orbital methods. XII. Further extensions of Gaussian—Type basis sets for use in molecular orbital studies of organic molecules. *J. Chem. Phys.* **1972**, *56*, 2257–2261. [CrossRef]
100. Tomasi, J.; Mennucci, B.; Cammi, R. Quantum mechanical continuum solvation models. *Chem. Rev.* **2005**, *105*, 2999–3093. [CrossRef]
101. Kumar, D.; Sastry, G.N.; de Visser, S.P. Effect of the axial ligand on substrate sulfoxidation mediated by iron(IV)-oxo porphyrin cation radical oxidants. *Chem. Eur. J.* **2011**, *17*, 6196–6205. [CrossRef]
102. Yang, T.; Quesne, M.G.; Neu, H.M.; Cantú Reinhard, F.G.; Goldberg, D.P.; de Visser, S.P. Singlet versus triplet reactivity in an Mn(V)-Oxo species: Testing theoretical predictions against experimental evidence. *J. Am. Chem. Soc.* **2016**, *138*, 12375–12386. [CrossRef]
103. Cantú Reinhard, F.G.; Faponle, A.S.; de Visser, S.P. Substrate sulfoxidation by an iron(IV)-oxo complex: Benchmarking computationally calculated barrier heights to experiment. *J. Phys. Chem. A* **2016**, *120*, 9805–9814. [CrossRef] [PubMed]
104. Cantú Reinhard, F.G.; Sainna, M.A.; Upadhyay, P.; Balan, G.A.; Kumar, D.; Fornarini, S.; Crestoni, M.E.; de Visser, S.P. A systematic account on aromatic hydroxylation by a cytochrome P450 model Compound I: A low-pressure mass spectrometry and computational study. *Chem. Eur. J.* **2016**, *22*, 18608–18619. [CrossRef] [PubMed]